Electronic Supplementary Material (ESI) for Nanoscale.
This journal is © The Royal Society of Chemistry 2020

Supporting Information:

Influence of $4f$ filling on electronic and magnetic properties in rare earth-Au surface compounds

L. Fernandez,[†,‡] M. Blanco-Rey,[¶,§] R. Castrillo-Bodero,[‡,§] M. Ilyn,[‡,§] K. Ali,[‡,§] E. Turco,[‡] M. Corso,[‡] M. Ormaza,[†] P. Gargiani,[‖,‡] M.A. Valbuena,[⊥,#] A. Mugarza,[⊥,@] P. Moras,[△] P. M. Sheverdyaeva,[△] A. K. Kundu,[△] M. Jugovac,[△] C. Laubschat,[▽] J.E. Ortega,[†,‡] and F. Schiller[*,‡]

† *Departamento de Física Aplicada I, UPV/EHU, 20018 San Sebastián, Spain*

‡ *Centro de Física de Materiales (CSIC-UPV-EHU) and Materials Physics Center (MPC), 20018 San Sebastián, Spain*

¶ *Departamento de Física de Materiales, UPV/EHU, 20018 Donostia-San Sebastián, Spain*

§ *Donostia International Physics Center, 20018 Donostia-San Sebastián, Spain*

‖ *ALBA Synchrotron Light Source, 08290 Cerdanyola del Vallès, Spain*

⊥ *Catalan Institute of Nanoscience and Nanotechnology (ICN2), CSIC and The Barcelona Institute of Science and Technology, Campus UAB, Bellaterra, 08193 Barcelona, Spain*

\# *IMDEA Nanociencia, 28049 Cantoblanco, Spain*

@ *ICREA, Institució Catalana de Recerca i Estudis Avançats, 08010 Barcelona, Spain*

△ *Instituto di Struttura della Materia, Consiglio Nazionale delle Ricerche, 34149 Trieste, Italy*

▽ *Institut für Festkörperphysik, TU Dresden, 01062 Dresden, Germany*

E-mail: frederikmichael.schiller@ehu.eus

Calculation of lattice constants

The lattice constants of rare-earth (RE) noble metal (NM) surface compounds that present a moiré lattice can be extracted either from LEED or from STM images. Often LEED images are too small with large superstructures to obtain lattice constants with small error values. On the other side STM images are usually taken on a small scale, where local effects can deviate the results due to impurities, lattice failure, etc. Furthermore possible thermal or electronic drift has to be considered. Here we will show the method applied to calculate the lattice constants independent of these effects. First, one has to search large scale images as the ones shown in Fig. 1 of the main manuscript that do not show lattice distortions. Then a smaller region without defects will be used that reveals both atomic resolution as well as the moiré superstructure. One can now either use Fast Fourier Transform (FFT) tools applied to these images or simply count over a large scale the atom arrangement inside the moiré lattice in all three main directions taking into account the $(\sqrt{3} \times \sqrt{3})$R30° lattice of the surface compound. Both methods will then give a factor F of the atomic arrangement to the superstructure, e.g., 1:12 in the case of $\mathrm{HoAu_2}$. Since the STM gives us the relation of the superstructure with respect to the surface compound, the superstructure denomination is then $([F{+}1]\times[F{+}1])$R30°, in the case of $\mathrm{HoAu_2}$ this results in (13×13)R30°. The RE-$\mathrm{NM_2}$ lattice constant can then be calculated by taking into account the underlying substrate bulk lattice constant. The last point is important since some pure materials like Au reveal alterations of their surface lattice, like the herringbone reconstruction. For Au we use the fcc lattice constant of $a = 4.09$Å. The interatomic distance in the (111) plane is $a/\sqrt{2} = 2.89$Å. Together with the above mentioned superstructure we immediately obtain the superlattice constant $L = (F + 1) \cdot a/\sqrt{2}$, which in the case of $\mathrm{HoAu_2}$ is L=37.6Å. One can verify this distance in the STM images. Next, the lattice constant of the RE-$\mathrm{NM_2}$ superlattice $b_{\text{RE-NM}}$ can be finally calculated as

$$b_{\text{RE-NM}} = \frac{L}{F}\sqrt{3} = \frac{F+1}{F}\sqrt{\frac{3}{2}}a \tag{1}$$

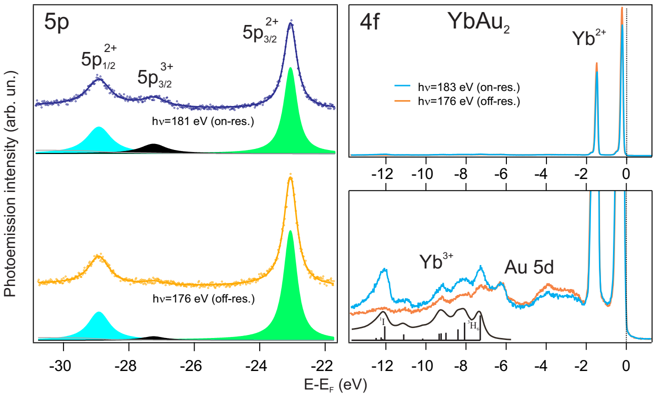

Figure S1: Photoemission spectra of the $5p$ and $4f$ core levels and valence bands of $\mathrm{YbAu_2}$, in off- and on-resonant photoemission, respectively. For the fit three Doniach-Sunjic line shapes[S1] have been used convoluted by a gaussian to account for the resolution of the experimental setup. The black spectrum denotes the atomic trivalent multiplet from S2.

For $\mathrm{HoAu_2}$ one obtains a lattice constant of $b_{HoAu_2} = 5.43$Å. In the case of $\mathrm{GdAu_2}$ an average (12.5×12.5)R30° superstructure leading to $b_{GdAu_2} = 5.44$Å was observed. The $\mathrm{YbAu_2}$ superstructure determined as (12.6×12.6)R30° yields the same value of $b_{YbAu_2} = 5.44$Å.

Photoemission results

Analysis of mixed-valent behavior in $\mathrm{YbAu_2}$

A detailed analysis of the mixed valence behavior of Yb is presented in Fig. S1. First we carried out fitting of the photoemission spectra in the Yb $5p$ core level spectra in on- and off resonant photoemission at the 4d→4f absorption edge. Resonant photoemission refers here only to the trivalent configuration of the Yb atoms since such a resonant process requires an unoccupied $4f$ level that is not available in the full $4f$ shell of divalent Yb. After photoexcitation, the decay of the $4d$ hole is predominantly through autoionization leading to a one-hole final state $5s^{-1}$ or $5p^{-1}$ or through normal Auger processes. Autoionization processes are strong on the low energy side of the resonance leading to strong enhancement of the photoemission peak at energies slightly below the giant resonance.[S3] This situation allows us to carry out a peak fit analysis for the on-resonant photoemission of the $5p$ part of the spectrum at hν = 181 eV. The fit yields the exact peak positions, widths, asymmetries and Shirley backgrounds of the Yb^{2+} and Yb^{3+} emissions. These parameters are then fixed to fit the off-resonant photoemission spectrum at hν = 176 eV. This procedure gives the intensity ratio of the di- and trivalent contributions in the off-resonant spectra. We extract the $5p_{3/2}^{2+}$ and $5p_{3/2}^{3+}$ peak positions at E-E_F=-23.06 eV and -27.24 eV, respectively. The average Yb valency value $\overline{\nu}$ is determined by evaluating the integral spectral weight corresponding to the photoemission intensity of the $5p_{3/2}$ peaks I^{2+} and I^{3+} as[S4–S6]

$$\overline{\nu} = 3 - \frac{I^{2+}}{I^{2+} + I^{3+}} \tag{2}$$

leading to $\overline{\nu}$=2.059. In principle a similar fit can be carried out for the $4f$ levels, nevertheless, the strong influence of the $5d$ levels of gold leads to a rather large error in the process.

If we would assume that the trivalent contribution of the photoemission spectrum originates from Yb atoms diffused into the bulk as “impurities” then these atoms would have a larger effective Au atom coordination with respect to a $YbAu_2$ bulk compound. Let us estimate the effect for a $YbAu_5$ compound and calculate its chemical shift (CS) with the Miedema scheme.[S7,S8] First we will calculate the CS of Yb in bulk $YbAu_2$ compared to trivalent Yb metal atoms. The CS is calculated as the difference between the formation enthalpies of the final and initial states. For the final state we take $HfAu_2$ (substitution of Yb^{3+} with Hf^{3+}), the initial state is approximated by $LaAu_2$ (substitution of Yb^{3+} with La^{3+}). The difference for the formation enthalpies can be calculated[S9] as 0.20 eV/molecule. We need the CS per atom, therefore we have to divide by the RE metal concentration inside that hypothetical $YbAu_2$ molecule and obtain a CS of 0.60 eV per Yb atom to higher binding energies. Now, one can do the same approximation for $YbAu_5$ that gives a CS of 0.125 eV/molecule and hence a CS of 0.75 eV per Yb atom. Therefore a possible core level shift of Yb impurities (as in $YbAu_5$) with respect to Yb in bulk $YbAu_2$ would result in a 0.15 eV shift to higher binding energies. This is much lower than the observed shift of approx. 1 eV

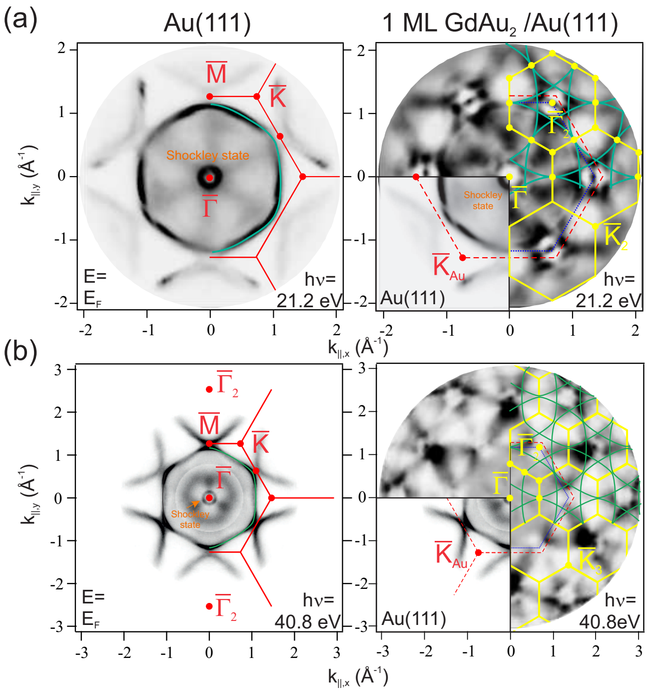

Figure S2: Angle-resolved photoemission (ARPES) maps for Au(111) (left) and 1 ML GdAu$_2$ (right), acquired at $E{=}E_F$ as a function of $k_{\|,x}$ and $k_{\|,y}$. The constant energy surfaces at the Fermi energy E_F are measured with the HeIα (21.2 eV, center) and He IIα (40.8 eV, right) excitation lines. On the right side of the images, the $(13/12 \cdot \sqrt{3} \times 13/12 \cdot \sqrt{3})$R30° surface Brillouin zones appear indicated with yellow lines, whereas the red dotted line marks the original (1×1) Au(111) surface unit cell and the dotted blue line represent the (13/12×13/12) surface Brillouin zone. Au $s-p$ band replica are marked with green lines in the the first quarter of each panel.

of our measurement with respect to the bulk component in YbAu$_2$$^{\text{S10}}$ and excludes that the here observed trivalent component arises from Yb bulk impurities.

Fermi energy crossings

Fig. S2 displays constant energy surfaces, namely photoemission intensity maps in momentum-space, at E_F for Au(111) (left column) and the GdAu$_2$ alloy (right) measured with 21.2 eV (center) and 40.8 eV (right) photon energies. For GdAu$_2$, the corresponding band dispersion along the high symmetry $\overline{\Gamma M}$ line is shown in the top panel of Fig. 4 of the main text, were A, B, C and C' name the different bands following Refs. S11,S12. For the Au(111) constant energy surfaces in Fig. S2, we mark the (1×1) surface Brillouin zone (in red) on

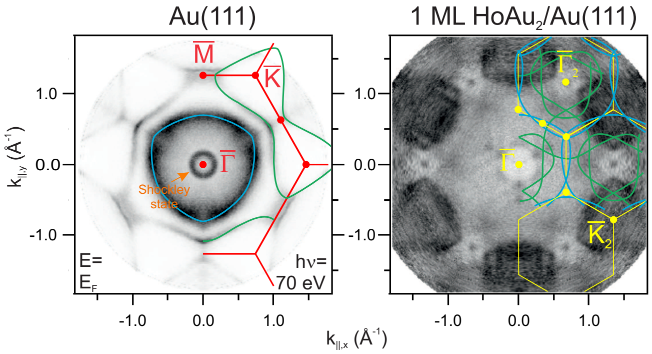

Figure S3: Angle-resolved photoemission (ARPES) maps for Au(111) (left) and 1 ML $\mathrm{HoAu_2}$ (right), acquired at $E{=}E_F$ as a function of $k_{\parallel,x}$ and $k_{\parallel,y}$. The constant energy surfaces at the Fermi energy E_F are measured with hν=70eV. On the right side of the images, the $(13/12\cdot\sqrt{3}\times 13/12\cdot\sqrt{3})$R30° surface Brillouin zones appear indicated with yellow lines. Au s,p band replica from the dog-bone feature and the triangular shaped structure are marked with green and light blue lines, respectively. Both features would result in the backfolded bands indicated in the first quarter of the $\mathrm{HoAu_2}$ panel. The star-like shape of band features around $\bar{\Gamma}_2$ in the experiment cannot be created from these backfolded bands.

the right hand side of each panel, and draw a green line over the Au $s-p$ bulk band, which crosses E_F near high symmetry $\overline{K}$ and $\overline{M}$ points. For the Fermi energy intensity mapping taken at $h\nu = 21.2$ eV, all spectral features observed in the Au case, including the Shockley surface state,[S13] are identical to those found in previous publications[S14] and very similar to the case of Ag(111)[S15] that is isoelectronic to Au and has the same lattice constant. After the formation of the $\mathrm{GdAu_2}$ monolayer a new surface Brillouin zone emerges. The Fermi surface at both photon energies mirrors the symmetry of the topmost layer of the alloy in its surface Brillouin zone, marked with yellow lines. With respect to the Au(111) plane, the periodicity strictly corresponds to a $(13/12\cdot\sqrt{3}\times 13/12\cdot\sqrt{3})$R30° structure, arising from the interference of the $(\sqrt{3}\times\sqrt{3})$R30° atomic reconstruction of the original Au(111) surface (red dotted lines) and the (13×13)-on-(12×12) coincidence moiré, the latter marked by blue dotted lines. The Fermi surface in $\mathrm{GdAu_2}$ is dominated by triangular features of low intensity around the $\bar{K}$ points and high intensity star-like shaped structures around higher-order $\bar{\Gamma}$-points, both, in reality originate from the Au-like $s-p$ band umklapp replicas inside the $(13/12\cdot\sqrt{3}\times 13/12\cdot\sqrt{3})$R30° surface Brillouin zone. This band-folding process is represented by the green lines in Fig. S2, which lead to hexagonal patterns of triangular objects around the second order $\overline{\Gamma}$-points at E_F. On the other hand, the direct inspection of $GdAu_2$ bands in Fig. 4 of the main text indicates that the Au-like $s-p$ emission that shapes the Fermi surface corresponds to the so-named C' band.[S11,S12] For the second photon energy used here the situation is very similar. At $h\nu = 40.8$ eV the Fermi crossing of the sp band in Au(111) is similar but not identical to the one observed at $h\nu$=21.2 eV. Umklapp bands into the new surface Brillouin zone for 1 ML $GdAu_2$/Au(111) correspond again very well to the star-like shape observed here. The star-like shape of the band crossing features can also be observed in the theoretic simulations of the Fermi energy crossings shown in Fig. S11, specially in the simulation of the surface compounds on a single Au substrate layer.

All these observations suggest that the star-like shape feature best observed around the higher-order $\bar{\Gamma}$-points are caused by the umklapp bands of the Au sp-band. Nevertheless, one has to remember that this band is a Au bulk band that disperses with the wave-vector k_z perpendicular to the surface. This situation can be seen when analyzing Fermi energy crossings in pure Au(111) at higher photon energies as the one shown in Fig. S3. Due to the higher photon energy, the k_z value increases and one cuts the three-dimensional Fermi surface at a different k position. The Fermi surface in Au is not a simple sphere as in the alkali metals but is connected around the L-points of the three-dimensional Brillouin zone. A cut at these connections leads to the situation that one observes here at $h\nu$=70 eV giving rise to the dog-bone like features (green in Fig. S3) and to the triangular shaped feature around the $\bar{\Gamma}$-point (light blue). Now, after the construction of the umklapp bands into the new $(13/12 \cdot \sqrt{3} \times 13/12 \cdot \sqrt{3})$R30° surface Brillouin zone the sp backfolded Fermi energy crossings are not anymore star-like shaped around the $\bar{\Gamma}$ points. Comparison to the band mapping of $HoAu_2$ surface compound at $h\nu$=70 eV shown in Fig. S3 reveals that the above suggested simple umklapp scenario of the substrate s, p band does not work anymore. The star-like shape of Fermi energy crossings of the band(s) around $\bar{\Gamma}$ is therefore caused by a true two-dimensional band.

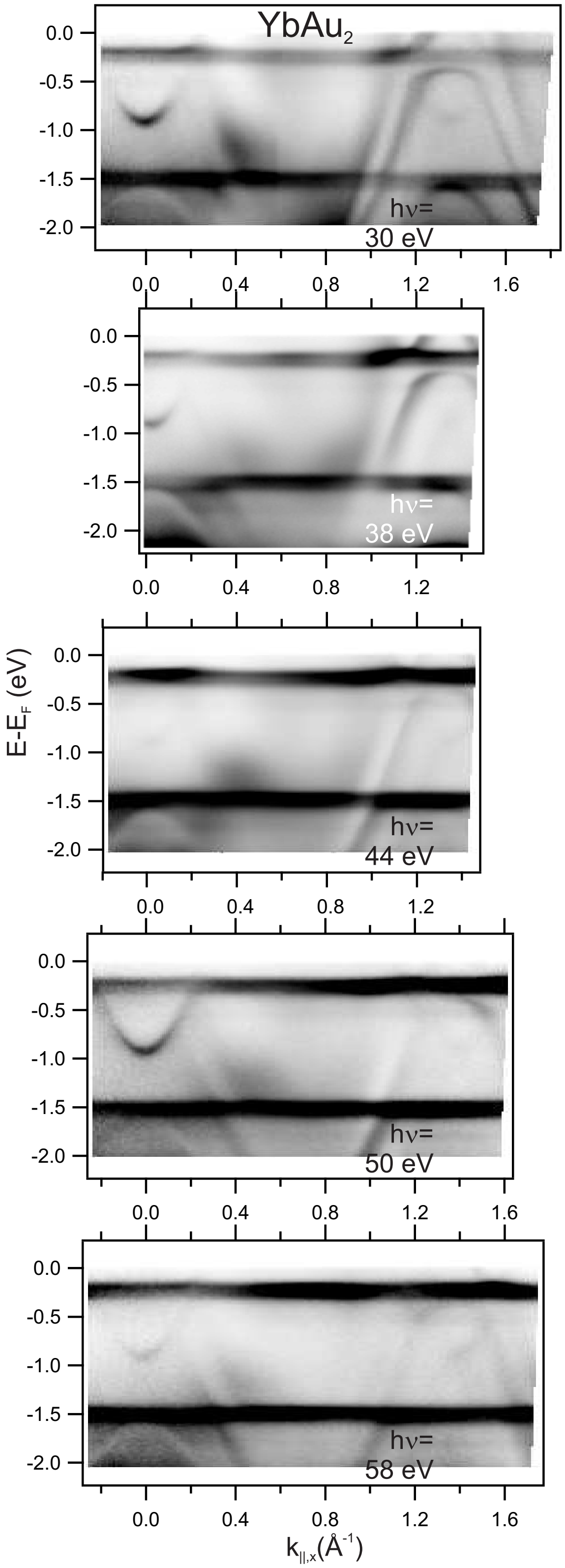

Figure S4: Photoemission intensity plots along the $\bar{\Gamma}\bar{M}\bar{\Gamma}$ direction of YbAu$_2$.

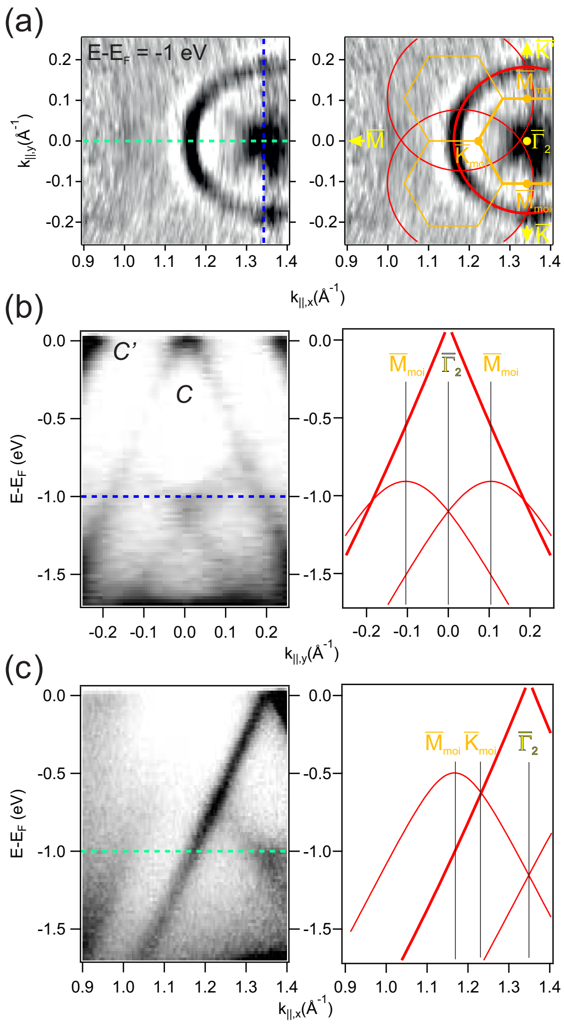

Figure S5: Photoemission intensity plots for $HoAu_2$ taken at $h\nu = 44$ eV. (a) Constant energy surface mapping (second derivative) at $E - E_F =$ -1eV around the $\bar{\Gamma}_2$-point of the second $(\sqrt{3}\times\sqrt{3})$R30° surface Brillouin zone (left), and the same with superimposed band dispersion in the moiré Brillouin zones and the two neighboring moiré lattices. Also shown are the moiré Brillouin zones itself. (b),(c) Cuts of the electronic bands along the vertical, horizontal lines in (a) along the $\bar{K}\bar{\Gamma}\bar{K}'$ and $\bar{\Gamma}\bar{M}\bar{\Gamma}_2$ Brillouin zones of the $(\sqrt{3} \times \sqrt{3})$R30° structure, respectively, corresponding to the $\bar{M}\bar{\Gamma}\bar{M}$ and $\bar{K}\bar{\Gamma}\bar{K}$ directions in the moiré Brillouin zone. Note that the $(\sqrt{3} \times \sqrt{3})$R30° and moiré lattices are rotated to each other by 30°.

Photoemission intensity plots for $YbAu_2$

Additional photoemission results for different photon energies of $YbAu_2$ are shown in Fig. S4. The two-dimensional band structure is well observed in the energy range between the Fermi level and $E - E_F =$ -2 eV binding energy. The photoemission intensity plots of $YbAu_2$ are taken for the indicated photon energies at $T = 17$ K. Measurement direction is along the

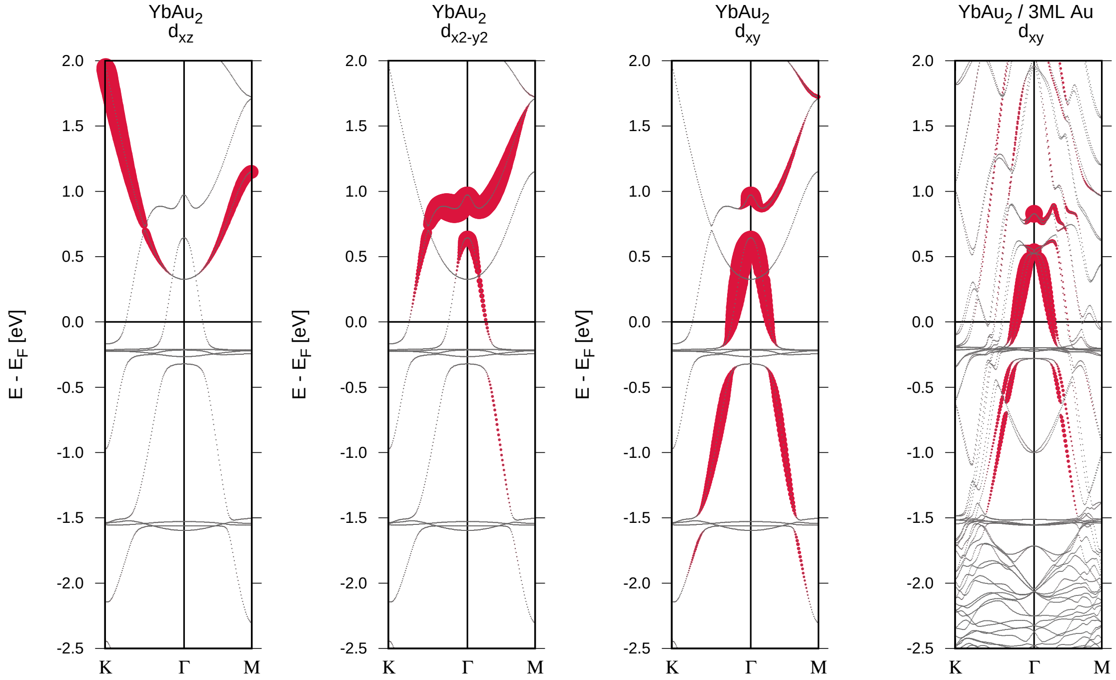

Figure S6: From left to right, detail of the theoretical Yb-d_{xz}, D (Yb-$d_{x^2-y^2}$) and C (Yb-d_{xy}) bands in the free-standing YbAu$_2$ monolayer and C for the YbAu$_2$ monolayer on three Au(111) layers. The size of the red features represents the amount of the corresponding Yb$-d$ orbital character in those states. Energies are referred to the Fermi level E_F.

$\bar{\Gamma}\bar{M}\bar{\Gamma}_2$ direction of the surface Brillouin zone.

Moiré umklapp bands in the surface compound

Umklapp bands from the C band due to the moiré superstructure are visible in the HoAu$_2$ as well as the YbAu$_2$ surface compounds at the $\bar{\Gamma}$-points of the second surface Brillouin zones as a “X”-like feature at approx. $E - E_F$ = -1.2 eV (see Fig. 3 of the main text and Fig. S4). Constant energy surfaces (CES) help to distinguish the umklapp from the nearby A and C' bands. In the CES of HoAu$_2$ taken for a photon energy $h\nu$ = 44 eV at $E - E_F$ = -1 eV shown in Fig. S5(a) one observes an intense ring caused by the C band and two less intense ring sectors. In order to check if these less intense features correspond to umklapp bands we simulate the C band by an anisotropic shape of a cone with

$$E = 0.1eV - 6.5\left(|k| - 0.35k^2\right) \tag{3}$$

around the $\bar{\Gamma}_2$ point of the $HoAu_2$ $(\sqrt{3}\times\sqrt{3})$R30° surface Brillouin zone, that also corresponds to the center of the small moiré Brillouin zone. We mark the simulated C band with thick red lines. A movement of the simulated C band into the two indicated neighboring moiré Brillouin zones lead to the band dispersion on the right hand site of S5, marked with thin red lines. The observed and simulated band structure coincide relatively well confirming the described umklapp scenario. The differences in the intensity of the replica and the absence of other umklapps can be related to the diffraction effects suffered by the outgoing electrons of the valence band.[S16]

Orbital character of bands

Fig. S6 shows the orbital character of some of the relevant bands in Fig. 5 of the main paper, calculated in the PBE approach.[S17] The two left-hand panels show for free-standing $YbAu_2$ the upward dispersing band with mainly Yb$-d_{zx}$ character and the D band of Yb$-d_{x^2-y^2}$ character. The latter band hybridizes near the zone center with the downward dispersing band labeled C, of mainly Yb$-d_{xy}$ character. In the free-standing $YbAu_2$ the C and the $4f$ bands show a significant hybridization. In the supported system, where hybridization with the substrate generates additional downward dispersive bands, the clear d_{xy} character of C is kept (right panel).

Both $4f_{5/2}$ and $4f_{7/2}$ band manifolds depart from the flat dispersion expected from a $4f$ orbital. The hybridized states are clearly contributed by electrons of $4f_{x(x^2-3y^2)}$ and $4f_{y(3x^2-y^2)}$ orbital symmetry. Fig. S7 shows the $4f$ bands that lie near the Fermi level in free-standing $YbAu_2$ in the PBE approach, where a degree of $4f$ character of those two specific symmetries is found in the C band nearby the band crossings. Thus, the dispersive

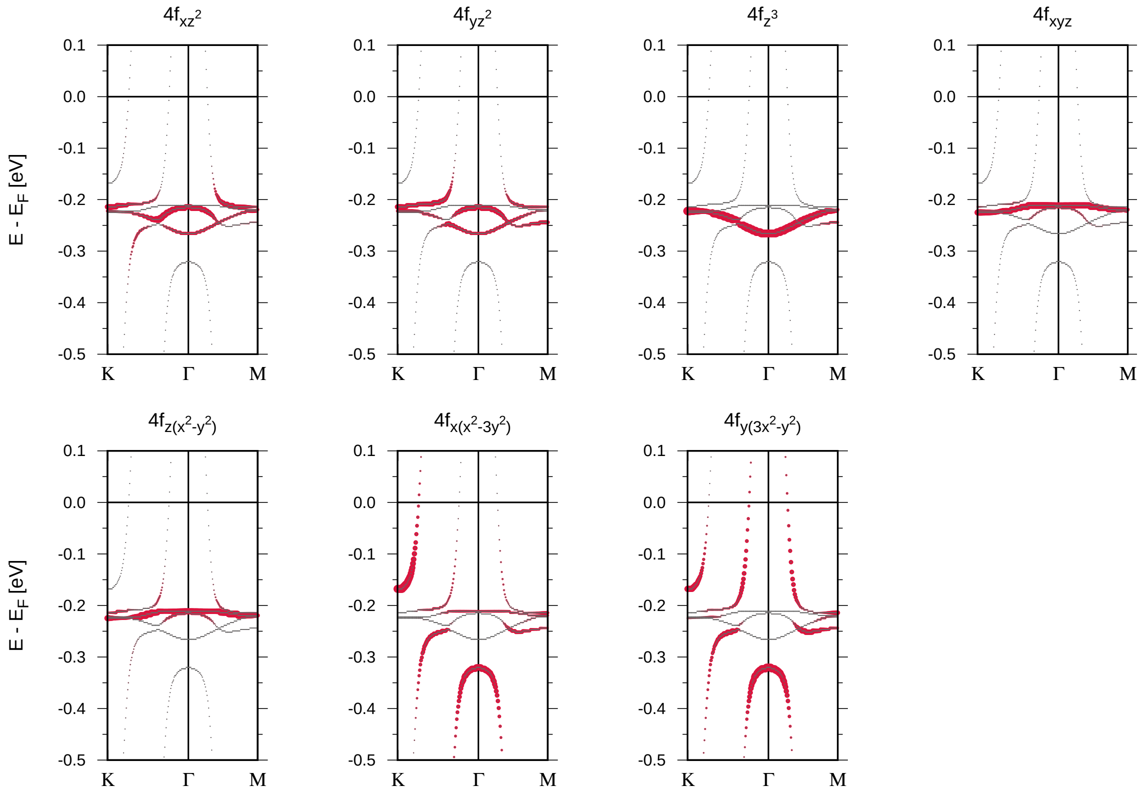

Figure S7: Detail of the $4f_{7/2}$ band manifold energy region calculated for free-standing YbAu$_2$. The size of the red features represents the amount of $4f$ orbital characters with the symmetries indicated in the labels (the notation corresponds to the general $4f$ set). Energies are referred to the Fermi level E_F.

character of the Yb$-d$ electrons facilitates the hybridization with the $4f$ electrons. A non-negligible contribution of $4f_{x(x^2-3y^2),y(3x^2-y^2)}$ also exists at the upward dispersing band from the K point at a binding energy of -0.25 eV, which has *sp* character. Finally, note that the results shown in Fig. S7 correspond to calculations where the spin quantization axis is perpendicular to the surface. With an in-plane axis the $4f$ band splittings are different as expected (not shown), but the qualitative picture of Yb$-d_{xy}-4f_{x(x^2-3y^2),y(3x^2-y^2)}$ dispersive hybrid states remains the same.

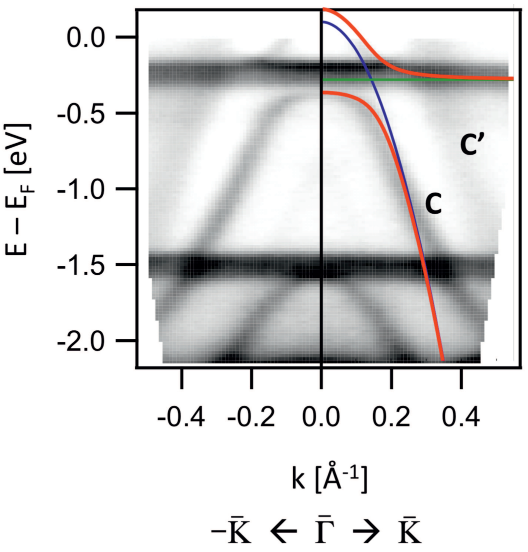

Figure S8: The ARPES band dispersion in the $\bar{K}\bar{\Gamma}\bar{K}$ direction is shown in the background. The red curves correspond to the renormalized band of Eq. 4, the blue curves to the parabolic model for the non-interacting C band and the green horizontal line to the non-interacting $4f$ level.

Hybridization model for YbAu$_2$

The anticrossing feature between the $4f_{7/2}$ manifold and the upward-dispersing C band for the YbAu$_2$ monolayer on Au(111) can be interpreted in terms of a model that includes a linear coupling term between those states and neglects correlation. This model results in the renormalized dispersion relation[S18]

$$E(k) = \frac{1}{2}\Big(\epsilon_{4f} + E_d(k) \pm \sqrt{(E_d(k) - \epsilon_{4f})^2 + 4V^2}\Big) \tag{4}$$

where ϵ_{4f} and $E_d(k)$ represent the non-interacting $4f$ and C band states, respectively, and V is the coupling strength. According to this model, it is possible to obtain continuous transitions to another valence state by shifting the $4f$ level. With a parabolic model for the C band $E_d(k) = \epsilon_d - ak^2$, which implies a constant density of states $\rho = \frac{1}{2\pi a}$ when integrated in two dimensions, we obtain qualitative agreement in the anticrossing region near the Fermi level in the $\bar{\Gamma}\bar{K}$ direction by using the empirical parameters $\epsilon_d = 0.085\,\mathrm{eV}$ $a = 18.5\,\mathrm{eV\AA^2}$, $V = 0.2\,\mathrm{eV}$ and $\epsilon_{4f} = -0.3\,\mathrm{eV}$ (see Fig. S8). A linewidth estimate can be extracted from the

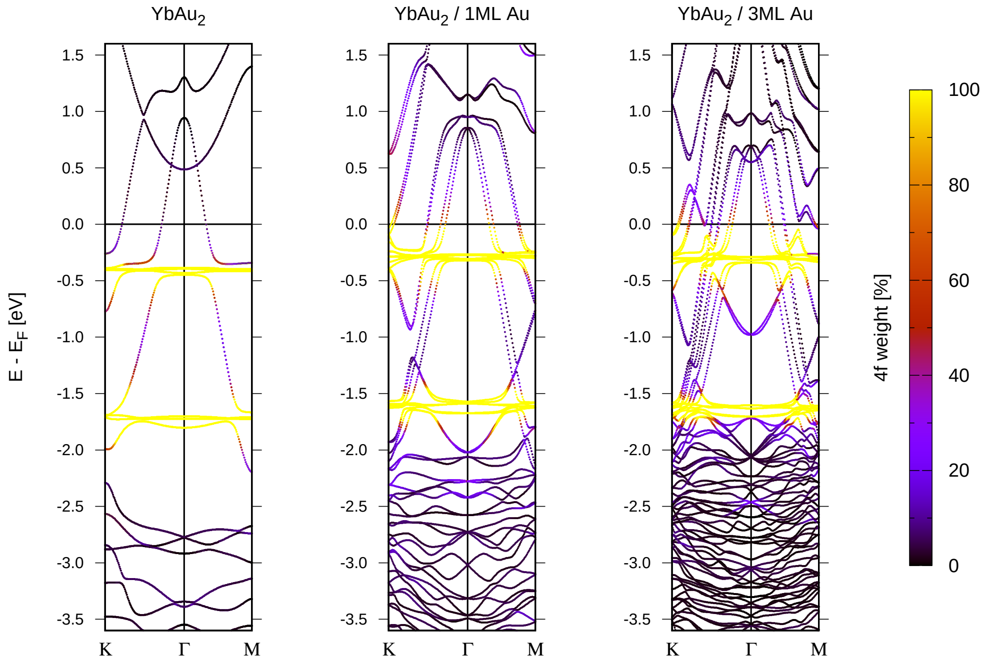

Figure S9: Calculated band structures in the PBE+U approach with $U = 3.5\,\text{eV}$ for a free-standing YbAu$_2$ monolayer (left), a YbAu$_2$/1ML Au(111) bilayer (center), and the YbAu$_2$/3ML Au(111) supported structure. The color scale represents the amount of $4f$ orbital character in those states. Energies are referred to the Fermi level E_F.

expression $\Gamma = \pi\rho V^2$ that results in a lifetime of approximately 0.25 ps. Note that this is a coarse estimate, which could be interpreted as an upper bound of the actual lifetime.

Correlation effects: calculations in the PBE+U approach

The effect of the Au substrate on the bandstructure of YbAu$_2$ in the PBE+U approach[S19,S20] is shown in Fig. S9, where correlation parameters $U = 3.5\,\text{eV}$ and $J = 0.5\,\text{eV}$ have been used on the $4f$ atomic orbital of Yb in the fully localized limit formulation.[S21] The main correlation effect on the $4f$ bands is a downward shift in the binding energies of about 0.1 eV, which reduces the spread above the Fermi level of the hybrid bands with partial $4f$ character. The addition of the correlation term also causes a subtle increase in the $4f$ bandwidths of both

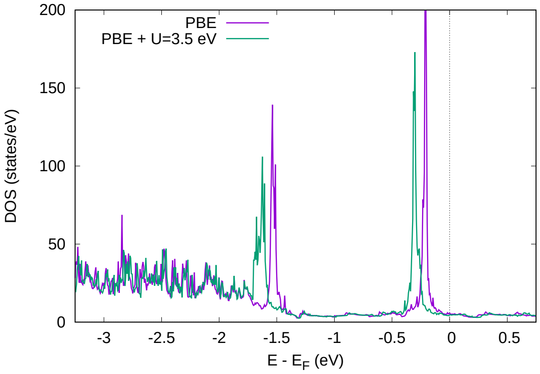

Figure S10: Total density of states (DOS) for the $YbAu_2$/3ML Au(111) stack calculated within the PBE and PBE+U approaches, where $U = 3.5$ eV. Energies are referred to the Fermi level E_F.

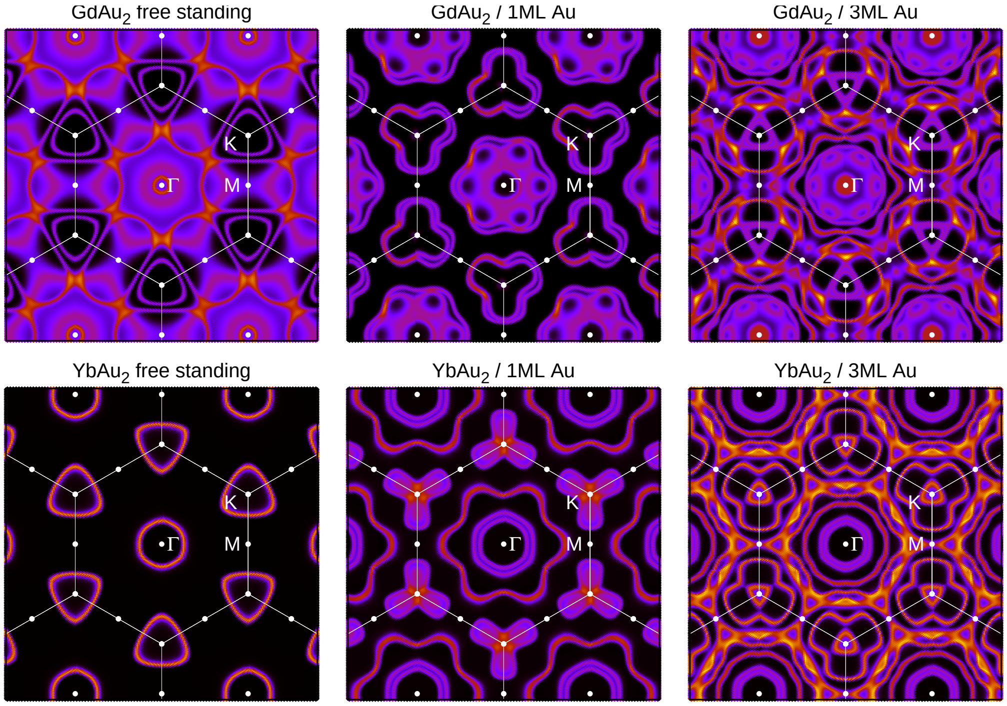

Figure S11: Theoretical Fermi surface maps of unsupported and supported $GdAu_2$ and $YbAu_2$. The states density colour gradient is obtained by using a gaussian of width 50 meV to account for the intensity contribution of each eigenenergy at $E = E_F$.

J-manifolds. The latter effect is better observed in the density of states of Fig. S10.

Calculated Fermi surface maps of $GdAu_2$ and $YbAu_2$

Figure S11 shows the Fermi surface (FS) maps of free standing and supported $GdAu_2$ and $YbAu_2$ model structures obtained from the band structures calculated from first principles. In the case of $GdAu_2$ (top panels) the band structures have been calculated with similar parameters as those used in the previous work by Ormaza *et al.*,[S22] this time keeping Gd spins in plane to match the experimentally observed magnetic anisotropy. The $YbAu_2$ maps (bottom panels) correspond to the band structure shown in Fig. 5c of the main paper.

The C band crossing at the Fermi level is easily identified in the free-standing $YbAu_2$ map as a sharp circle around the Γ point, whereas for $GdAu_2$ additional features appear as a consequence of the different valence state of the RE. The bright spots in the ΓK direction are due to a hybrid band of mainly Gd-$d_{x^2-y^2}$ character (D) showing upward dispersion, and the weaker background intensity results from a weakly dispersive hybrid band of Gd-$d_{xz,yz}$ character that lies very close the Fermi level (see Supplementary Figure 4 of Ref.[S22]). Note that the corresponding D and d_{xz} bands in $YbAu_2$ lie well above the Fermi level (Fig. 4c of the main paper).

The models with a 1 ML Au substrate (centre panels) show that the C' band appears by interaction with the substrate atoms. This band yields the same star-shaped feature surrounding the C band that is observed in the ARPES experiments of $YbAu_2$ (see Fig. 4c of the main paper). Both C and C' bands are observed in the $GdAu_2$/1 ML map, too, although they are again slightly blurred because of the Gd-$d_{x^2-y^2}$- and Gd-$d_{xz,yz}$-like bands crossing the Fermi level. Note that these $GdAu_2$ calculations are also representative of $HoAu_2$, as both REs are trivalent in these compounds.

Finally, the FS maps with 3 ML Au substrate are more intricate as many substrate bands cross the Fermi level. Still, the C circle and C' stars can be distinguished. If the substrate thickness were larger, these substrate contributions would tend to form a continuous background.

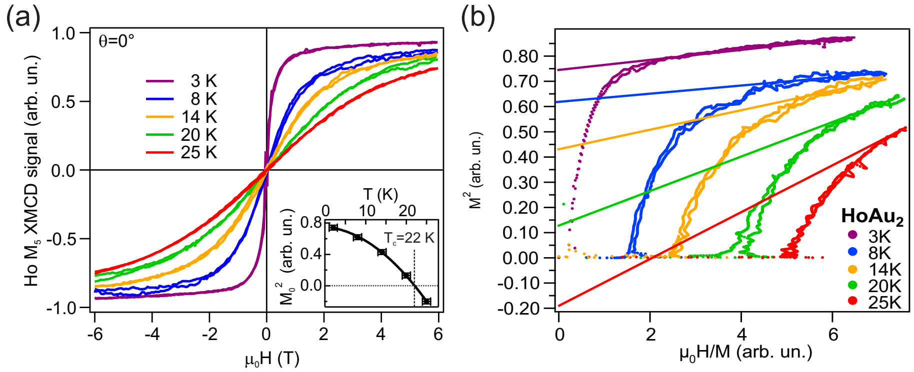

Figure S12: Arrot plot analysis of the XMCD magnetization curves in order to extract the Curie temperature T_C.

Magnetic measurements of HoAu$_2$

The magnetization axis of the θ=0° and θ=70° magnetization curves in Fig. 6 of the main text were scaled to the Ho atomic moment J_z=L_z+$S_z/2$ obtained by sum rules analysis[S23,S24] from the orbital L_z and spin S_z angular moments of the XMCD spectra. Sum Rules analysis give only rise to an effective spin magnetic moment

$$S_z^{eff} = 2S_z \cdot \left(1 + 3 \cdot \frac{T_z}{S_z}\right) \tag{5}$$

where the magnetic dipolar term T_z also needs to be considered. In order to account for T_z the quotient T_z/S_z=0.072 for Ho^{3+} was taken from ref. S25.

The Curie temperature T_C of XMCD data can be extracted by Arrot plot analysis[S22,S26] of the magnetization curves at different temperatures. Fig. S12 shows the corresponding analysis. There we plot M^2 vs $\mu_0 H/M$ and fit the high field data with a linear fit and search the M^2 value for $\mu_0 H/M = 0$, see Fig. S12(b). Next, we plot these M_0^2 values versus the temperature at which the magnetization curves were measured. A polynomial fit (here of second order) then reveals the Curie temperature when $M_0^2 = 0$.

Shape anisotropy of $GdAu_2$ and $HoAu_2$

The shape anisotropy of $GdAu_2$ and $HoAu_2$ is estimated from the classsical magnetic dipole-dipole interaction energy between spins on a two-dimensional hexagonal lattice,

$$E_{\mathrm{dip-dip}} = \frac{\mu_0}{4\pi} \sum_{i<j} \frac{\mathbf{S}_i \cdot \mathbf{S}_j - 3\left(\mathbf{S}_i \cdot \hat{R}_{ij}\right)\left(\mathbf{S}_j \cdot \hat{R}_{ij}\right)}{R_{ij}^5} \tag{6}$$

where $\mathbf{R}_{ij}$ are lattice vectors connecting the i-th and j-th spins, $\mathbf{S}_i$ and $\mathbf{S}_j$, respectively. In two dimensions the sum converges with the distance between spin pairs (we find that a cut-off distance of ~ 3000 Å is needed to converge energies in the μeV range). The difference in dipole-dipole energies of configurations with spins oriented perpendicular and in-plane is the shape anisotropy. Note that the dipolar interactions in the planar geometry favor in-plane anisotropy. For $GdAu_2$, with spin $S = 7/2$, this results in approximately 0.05 meV per Gd atom. Since the $HoAu_2$ lattice has the same geometry, using the atomic Ho value $S = 2$ the estimated shape anisotropy is reduced by a factor $(7/4)^2$.

References

(S1) Doniach, S.; Šunjic, M. Many-electron singularity in X-ray photoemission and X-ray line spectra from metals. *Journal of Physics C: Solid State Physics* **1970**, *3*, 285.

(S2) Gerken, F. Calculated photoemission spectra of the 4f states in the rare-earth metals. *Journal of Physics F: Metal Physics* **1983**, *13*, 703–713.

(S3) Sairanen, O. P.; Aksela, S.; Kivimaki, A. Resonance Auger and autoionization processes in solid lanthanum after 4d to 4f resonant excitation by synchrotron radiation. *Journal of Physics: Condensed Matter* **1991**, *3*, 8707–8714.

(S4) Moreschini, L.; Dallera, C.; Joyce, J. J.; Sarrao, J. L.; Bauer, E. D.; Fritsch, V.; Bobev, S.; Carpene, E.; Huotari, S.; Vankó, G.; Monaco, G.; Lacovig, P.; Panaccione, G.; Fondacaro, A.; Paolicelli, G.; Torelli, P.; Grioni, M. Comparison of bulk-sensitive spectroscopic probes of Yb valence in Kondo systems. *Phys. Rev. B* **2007**, *75*, 035113.

(S5) Kummer, K.; Kucherenko, Y.; Danzenbächer, S.; Krellner, C.; Geibel, C.; Holder, M. G.; Bekenov, L. V.; Muro, T.; Kato, Y.; Kinoshita, T.; Huotari, S.; Simonelli, L.; Molodtsov, S. L.; Laubschat, C.; Vyalikh, D. V. Intermediate valence in Yb compounds probed by $4f$ photoemission and resonant inelastic x-ray scattering. *Phys. Rev. B* **2011**, *84*, 245114.

(S6) Chatterjee, S.; Ruf, J. P.; Wei, H. I.; Finkelstein, K. D.; Schlom, D. G.; Shen, K. M. Lifshitz transition from valence fluctuations in $\mathrm{YbAl_3}$. *Nature Communications* **2017**, *8*, 2041.

(S7) de Boer, F.; Mattens, W.; Boom, R.; Miedema, A.; Niessen, A. *Cohesion in metals. Transition metal alloys*; North-Holland Amsterdam (Netherlands), 1988; Vol. 1.

(S8) Bakker, H. *Enthalpies in Alloys Miedema's Semi-Empirical Model*; Material Science Foundation; ttp Trans Tech Publications, 1998; Vol. 1.

(S9) Laubschat, C.; Kaindl, G.; Schneider, W.-D.; Reihl, B.; Mårtensson, N. Stability of 4f configurations in rare-earth-metal compounds. *Phys. Rev. B* **1986**, *33*, 6675–6683.

(S10) Wertheim, G. K.; Wernick, J. H.; Crecelius, G. Surface effects on valence in rare-earth intermetallic compounds. *Phys. Rev. B* **1978**, *18*, 875–879.

(S11) Corso, M.; Verstraete, M. J.; Schiller, F.; Ormaza, M.; Fernández, L.; Greber, T.; Torrent, M.; Rubio, A.; Ortega, J. E. Rare-Earth Surface Alloying: A New Phase for $\mathrm{GdAu_2}$. *Phys. Rev. Lett.* **2010**, *105*, 016101.

(S12) Ormaza, M.; Fernández, L.; Lafuente, S.; Corso, M.; Schiller, F.; Xu, B.; Diakhate, M.;

Verstraete, M. J.; Ortega, J. E. $LaAu_2$ and $CeAu_2$ surface intermetallic compounds grown by high-temperature deposition on Au(111). *Phys. Rev. B* **2013**, *88*, 125405.

(S13) Reinert, F.; Nicolay, G.; Schmidt, S.; Ehm, D.; Hüfner, S. Direct measurements of the L-gap surface states on the (111) face of noble metals by photoelectron spectroscopy. *Phys. Rev. B* **2001**, *63*, 115415.

(S14) Tusche, C.; Krasyuk, A.; Kirschner, J. Spin resolved bandstructure imaging with a high resolution momentum microscope. *Ultramicroscopy* **2015**, *159*, 520 – 529.

(S15) Greber, T.; Raetzo, O.; Kreutz, T. J.; Schwaller, P.; Deichmann, W.; Wetli, E.; Osterwalder, J. A photoelectron spectrometer for k-space mapping above the Fermi level. *Review of Scientific Instruments* **1997**, *68*, 4549–4554.

(S16) Srour, W.; Tejeda, A.; Nicolaou, A.; Le Fèvre, P.; Bertran, F.; Taleb-Ibrahimi, A.; Malterre, D. Experimental correlation between photoemission matrix elements and LEED intensities in superperiodic structures. *Journal of Electron Spectroscopy and Related Phenomena* **2012**, *185*, 441 – 447.

(S17) Perdew, J. P.; Burke, K.; Ernzerhof, M. Generalized Gradient Approximation Made Simple. *Phys. Rev. Lett.* **1996**, *77*, 3865–3868.

(S18) Lawrence, J. M.; Riseborough, P. S.; Parks, R. D. Valence fluctuation phenomena. *Reports on Progress in Physics* **1981**, *44*, 1–84.

(S19) Anisimov, V. I.; Aryasetiawan, F.; Liechtenstein, A. I. *J. Phys.: Condens. Matter* **1997**, *9*, 767.

(S20) Shick, A. B.; Liechtenstein, A. I.; Pickett, W. E. *Phys. Rev. B* **1999**, *60*, 10763.

(S21) Anisimov, V. I.; Solovyev, I. V.; Korotin, M. A.; Czyzyk, M. T.; Sawatzky, G. A. *Phys. Rev. B* **1993**, *48*, 16929.

(S22) Ormaza, M.; Fernández, L.; Ilyn, M.; Magaña, A.; Xu, B.; Verstraete, M. J.; Gastaldo, M.; Valbuena, M. A.; Gargiani, P.; Mugarza, A.; Ayuela, A.; Vitali, L.; Blanco-Rey, M.; Schiller, F.; Ortega, J. E. High Temperature Ferromagnetism in a GdAg2 Monolayer. *Nano Letters* **2016**, *16*, 4230–4235.

(S23) Thole, B. T.; Carra, P.; Sette, F.; van der Laan, G. X-ray circular dichroism as a probe of orbital magnetization. *Phys. Rev. Lett.* **1992**, *68*, 1943–1946.

(S24) Thole, B. T.; van der Laan, G. Sum rules for magnetic dichroism in rare earth 4f photoemission. *Phys. Rev. Lett.* **1993**, *70*, 2499–2502.

(S25) Teramura, Y.; Tanaka, A.; Thole, B.; Jo, T. Effect of Coulomb Interaction on the X-Ray Magnetic Circular Dichroism Spin Sum Rule in Rare Earths. *Journal of the Physical Society of Japan* **1996**, *65*, 3056–3059.

(S26) Arrott, A. Criterion for Ferromagnetism from Observations of Magnetic Isotherms. *Phys. Rev.* **1957**, *108*, 1394–1396.